2008

Parameter Estimation and Life Modeling of Lithium-Ion Cells

Shriram Santhanagopalan

Qi Zhang
University of South Carolina - Upstate, qhzhang@email.uscupstate.edu

Karthikeyan Kumaresan

Ralph E. White
University of South Carolina - Columbia, white@cec.sc.edu

Publication Info

Published in *Journal of the Electrochemical Society*, Volume 155, Issue 4, 2008, pages A345-A353.

Journal of The Electrochemical Society, **155** (4) A345-A353 (2008)
0013-4651/2008/155(4)/A345/9/$23.00 © The Electrochemical Society

Parameter Estimation and Life Modeling of Lithium-Ion Cells

Shriram Santhanagopalan,*[,a] Qi Zhang, Karthikeyan Kumaresan,** and Ralph E. White***[,z]**

Department of Chemical Engineering, University of South Carolina, Columbia, South Carolina 29208, USA

Lithium-ion pouch cells were cycled at five different temperatures (5, 15, 25, 35, and 45°C), and rate capability studies were performed after every hundred cycles. The data were used with a simple physics-based model to estimate parameters that capture the capacity fade in the cell, with cycling. The weight of active material within each electrode was estimated as a function of time, using rate capability data at the *C*/33 rate. The *C*-rate for these cells is 1.656 A. The capacity fade due to the loss of active material and that due to the loss of cyclable lithium were quantified. It was found that while the loss of cyclable lithium is the limiting cause for the capacity decay of the cell during the first 200 cycles, the loss of active carbon, which is the anode material, becomes limiting for these cells. The loss of active material leads to a drastic decrease in cell capacity at higher temperatures.
 [DOI: 10.1149/1.2839630]

Manuscript submitted October 24, 2007; revised manuscript received January 4, 2008. Available electronically March 7, 2008.

The lithium-ion cell is among the most popular candidates considered actively as a replacement for nickel-based batteries in automobile, small-electronics, satellite, and several other applications. This demand has fueled the need for improved performance and safety of the lithium-ion system. Consequently, a substantial amount of work has gone into understanding the mechanism of the capacity fade occurring in the battery experimentally and via rigorous theoretical analysis.[1-18] Elaborate mathematical models, including the charge-transfer reaction, electronic conduction, ionic conduction, and solution and solid phase diffusion have been proposed. Arora et al.[12] investigated the lithium deposition reaction. Ramadass and Ploehn et al. proposed a solvent reduction reaction at the anode during the charging of the cell. In some models, the reduction reaction was included as a side reaction to account for the capacity fade of a battery with cycling.[17,18] A semi-empirical model incorporating lumped parameters for capacity fade due to loss of lithium and the loss of active materials was also proposed.[19] Other investigators have used circuit analogs to model the degradation mechanism of the battery, wherein the change in an empirical parameter is followed as a function of time or cycle number in order to capture the loss of capacity.[14-16] Reports of the open-circuit voltage (OCV) changing as the cell ages also exist.[20]

Experimental investigations[21-24] have shown that the loss of capacity can be attributed to loss of active material,[19] degradation of the electrodes, decomposition or loss of electrolyte,[18] formation of films on the anode and/or the cathode,[6,7] increased impedance of the electrodes, dissolution of the current collector,[13] etc. The actual loss of capacity in a lithium-ion cell results from a combination of two or more of these factors. A rigorous theoretical study of the contribution from these factors is essential to understand the cycling behavior of the system and is critical in the development of models that can predict the life of the battery used in a particular application. In the present work, we have attempted to quantify the capacity fade due to the loss of cyclable lithium (in the form of side reactions, deposition of metallic lithium, etc.) and that due to the loss of active material (in the form of isolation, loss of contact, masking due to film formation, etc.) from discharge data of lithium-ion cells cycled at various rates.

Experimental

Lithium-ion pouch cells received from Mine Safety Appliances (MSA) were used for the cycling studies. The nameplate capacity of each cell is 1.656 Ah. Each cell consisted of four (two-sided) positive electrodes (cathodes) and five (three two-sided and two one-sided) negative electrodes (anodes). The active materials of the positive and negative electrodes are stoichiometric lithium cobalt oxide ($LiCoO_2$) and mesocarbon microbead 2528, respectively. One molar $LiPF_6$ in a quaternary solvent mixture of ethylene carbonate, propylene carbonate, ethyl methyl carbonate, and diethyl carbonate was used as the electrolyte. Each of the four two-sided positive electrodes was bagged using the separator (Celgard). Each of the three two-sided negative electrodes was sandwiched between two positive electrode-containing separator bags while the two single-sided negative electrodes covered the outer positive electrodes. The entire assembly of anodes, cathodes, and separators was enclosed by a proprietary material to make the pouch cell.

After the initial formation cycles, the cells were cycled at five different temperatures (5, 15, 25, 35, and 45°C). Each cycle consisted of a constant current charging at the *C*/2 rate (*C*-rate = 1.656 A) until the voltage reached an end-of-charge voltage of 4.1 V, a constant voltage charging at 4.1 V until the current tapered down to 50 mA, and a constant current discharge at the *C*/2 rate up to a cutoff voltage of 3.3 V. All cycling tests were done using Arbin BT-2000 battery testing systems (College Station, TX). Tenny environmental chambers (model T6S, Williamsport, PA) were used for maintaining respective cycling temperatures and near-zero humidity atmospheres. Rate capability tests were done before cycling and at the end of every 100 cycles. The rate capability tests consisted of measuring the charge–discharge capacity of the cell at three different rates, namely, *C*/33, *C*/2, and *C*, in that order. For the *C*/33 rate, the cell was first charged to 4.1 V and then discharged until the voltage reached 3.3 V. For *C*/2 and *C*-rates, cells were first charged to 4.1 V at the respective constant current rate followed by a constant voltage charging at 4.1 V until the current reached 50 mA. The subsequent discharge consisted of two stages. The first discharge was done at the respective rate (*C*/2 or *C*) until the voltage reached 3.3 V, followed by a rest period of 30 min. The second-stage discharge was done with a constant current of 50 mA (which is equal to the *C*/33 rate). The rate capability tests were done at the same temperature as that of cycling in order to analyze actual conditions prevailing inside a cell during cycling.

Mathematical Model

Detailed mathematical models describing various electrochemical phenomena in the lithium-ion cell exist in the literature.[2-4,12,17] We recently presented a comparison of several models and their suitability for studying the performance of the system under different operating conditions. In order to model the cycling performance of lithium-ion cells, Ramadass et al. proposed a side-reaction-based approach[17] wherein the loss in cell capacity was entirely due to the reduction of the solvent at the anode during charge. In utilizing this approach to fit cycling data, they found that the film formation approach was not adequate to capture the change in the profiles of the discharge curves with cycling. Empirical expressions for change of parameters like the diffusion coefficient and the resistance of the

* Electrochemical Society Active Member.
** Electrochemical Society Student Member.
*** Electrochemical Society Fellow.
[a] Present address: Celgard LLC, Charlotte, North Carolina 28273, USA.
[z] E-mail: white@engr.sc.edu

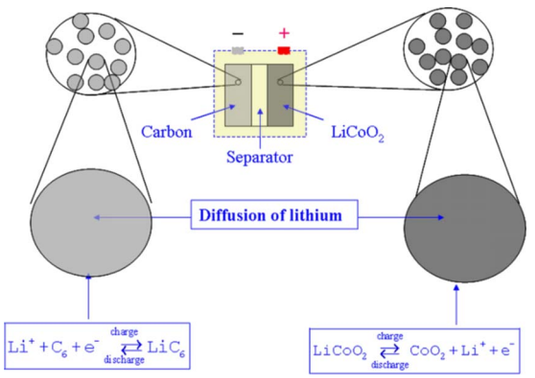

Figure 1. (Color online) Schematic representation of the single particle model.

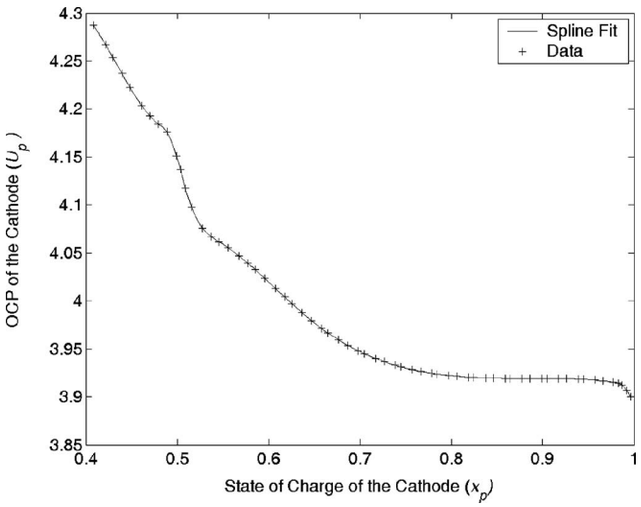

Figure 2. OCP curve for the cathode. The symbols indicate the experimentally measured data at the *C*/100 rate and the line represents the spline fit.

solid electrolyte interface layer were then proposed.[19] However, data from cycled MSA cells indicate that there is a loss of active material apart from the loss of lithium. The first step toward developing a physics-based model is to understand how parameters like the weight of the accessible active material and the state of charge within each electrode change as the cell ages.[4]

In the present work, a simple mathematical model[25,26] is used to estimate the active material loss in each electrode as well as the state of charge of each electrode at the end of every hundred cycles. Figure 1 presents a schematic illustration of a lithium-ion battery with an individual spherical particle representing each intercalation electrode. The model includes the assumption that each electrode in the cell can be modeled by a single particle, representative of the behavior of the entire electrode. Other assumptions used in this particle model are that the electrolyte concentration, c_e, is a constant throughout the battery (i.e., $c_e = 10^{-3}$ mol/cm^3 in the anode, separator, and cathode) and that the solid phase potential is uniform inside each electrode. With these assumptions, the reaction current density is also uniform in each electrode, and the electrochemical performance of a single intercalation particle of an electrode can be used to represent the performance of the entire electrode. Contributions from the solution phase to the cell voltage are assumed to be negligible, because the solution phase concentration is uniform. We demonstrated[26] the validity of these limitations in modeling charge/discharge curves at current values less than or equal to the 1 *C* rate.

The active material loading (i.e., the accessible weight of the active material) of electrode i, w_i, the density of the active material of electrode i, ρ_i, and the radius of the intercalation particle of electrode i, R_i, can be used to determine the electroactive surface area of electrode i, S_i, as follows

$$S_i = \frac{3}{R_i}\frac{w_i}{\rho_i}, \quad i = n,p \qquad [1]$$

where n stands for the negative electrode (carbon anode), and p stands for the positive electrode (lithium cobalt oxide cathode). Equation 1 is obtained based on the assumption that spherical intercalation particles of equal size (i.e., R_i) are used to make electrode i. The weight of each electrode w_i was treated as a parameter.

The equation that describes lithium-ion diffusion in the spherical intercalation particle (solid phase) of electrode i is given by Fick's second law

$$\frac{\partial \theta_i}{\partial t} = \frac{D_i}{R_i^2}\frac{1}{\bar{r}_i^2}\frac{\partial}{\partial \bar{r}_i}\left(\bar{r}_i^2\frac{\partial \theta_i}{\partial \bar{r}_i}\right), \quad i = n,p \qquad [2]$$

where $\theta_i = c_i/c_{i,max}$ is the state of charge (SOC) of electrode i (c_i is the concentration of lithium ions in the intercalation particle of electrode i, and $c_{i,max}$ is the maximum lithium-ion concentration in electrode i), D_i is the solid phase diffusion coefficient of lithium ions in electrode i, and $\bar{\bar{r}}_i = r/R_i$ is the normalized spherical coordinate (r is the dimensional coordinate of the spherical particle, and R_i is the radius of the intercalation particle in electrode i).

The initial condition for θ_i is

$$\theta_i|_{t=0,0\le\bar{r}_i\le1} = \theta_{i,0}, \quad i = n,p \qquad [3]$$

where $\theta_{i,0}$ is the stoichiometric fraction of lithium inside each electrode at the beginning of discharge. The values of $\theta_{i,0}$ are not known and, consequently, they are treated as parameters.

The boundary conditions for θ_i are

$$\left.\frac{\partial \theta_i}{\partial \bar{r}}\right|_{\bar{r}_i=0,t\ge0} = 0, \quad i = n,p \qquad [4]$$

and

$$-\left.\frac{D_i}{R_i}\frac{\partial \theta_i}{\partial \bar{r}}\right|_{\bar{r}_i=1,t\ge0} = \frac{J_i}{S_i c_{i,max}}, \quad i = n,p \qquad [5]$$

where J_i is the lithium-ion flux for the electrochemical reaction per unit surface area of the intercalation particle of electrode i and is related to the Butler–Volmer equation by

$$J_i = k_i c_{i,max}(1 - \theta_i|_{\bar{r}_i=1})^{0.5}\,\theta_i|_{\bar{r}_i=1}^{0.5} c_e^{0.5}\left\{\exp\left(\frac{0.5F}{RT}\eta_i\right) - \exp\left(-\frac{0.5F}{RT}\eta_i\right)\right\}, \quad i = n,p \qquad [6]$$

where k_i is the rate constant for the electrochemical reaction of electrode i, and η_i is the overpotential of electrode i

$$\eta_i = \Phi_{1,i} - U_i, \quad i = n,p \qquad [7]$$

where $\Phi_{1,i}$ is the solid phase potential of electrode i and U_i is the open-circuit potential (OCP) of electrode i (shown in Fig. 2 and 3). No attempt is made in this work to model the film growth due to a side reaction, because data at each cycle was fit separately. The predicted voltage of a cell is the difference between the solid phase potential of the cathode, $\Phi_{1,p}$, and the solid phase potential of the anode, $\Phi_{1,n}$

$$V_{Cell} = \Phi_{1,p} - \Phi_{1,n} \qquad [8]$$

The dependent variables in the particle model presented above are θ_p, η_p, θ_n, η_c, I, and V_{Cell}. If I is the control variable, the following equation will be used in the numerical calculation

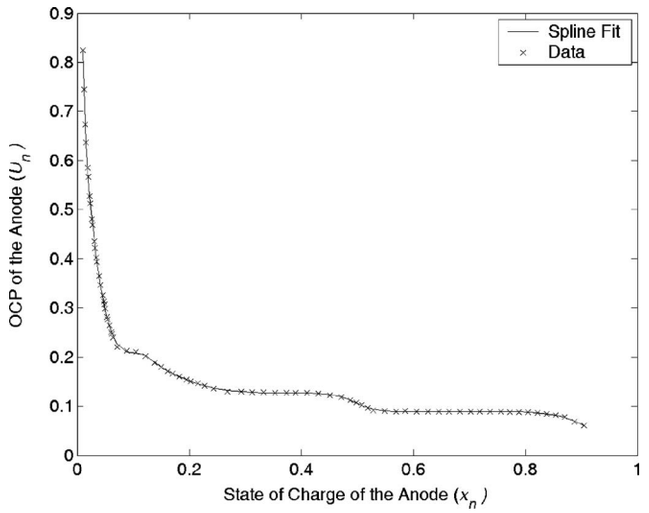

Figure 3. OCP curve for the anode. The symbols indicate the experimentally measured data at the *C*/10 rate and the line represents the spline fit.

$$I = I_{app} \quad [9]$$

where I_{app} is the applied current which can change with time or be a constant. If the cell potential $(\Phi_{1,p} - \Phi_{1,n})$ is the control variable, the following equation is used instead

$$\Phi_{1,p} - \Phi_{1,n} = V_{app} = V_{Cell} \quad [10]$$

where V_{app} is the applied voltage which is prespecified (this value can also change with time or be a constant). Equations 2-5 can be simplified using a polynomial approximation.[10,11]

A differential and algebraic equation (DAE) subroutine in Fortran called DASRT was used in our numerical calculation.[25] DASRT uses backward differentiation formulas of orders one through five to solve a system of equations of the form

$$\mathbf{F}(t, \mathbf{Y}, \mathbf{Y}') = 0 \quad [11]$$

where $\mathbf{Y}$ is the vector of dependent variables, and $\mathbf{Y}'$ is the vector of the first derivatives of dependent variables with respect to t. DASRT is an integration subroutine. It takes the values for $\mathbf{Y}$ and $\mathbf{Y}'$ at $t = t_1$ and returns the values for $\mathbf{Y}$ and $\mathbf{Y}'$ at $t = t_2$. DASRT advances the solution from t_1 to t_2 using step sizes automatically selected to achieve a specified accuracy. This feature is particularly useful in the estimation of parameters, because the values for the dependent variables, and their derivatives with respect to the array of parameters, needs to be obtained precisely at the instant of time for which the experimental data point is available. An initialization subroutine called DAEIS[27] developed in our group was used along with DASRT to provide consistent values for $\mathbf{Y}$ and $\mathbf{Y}'$ at $t = 0$ and at every occurrence of a discontinuity. In addition to the high accuracy and efficiency in handling DAEs, DASRT also features the detection of zero crossing for one or more special constraint equations.

Parameter Estimation

The values for some electrode and electrolyte properties such as $c_{i,max}$, R_i, w_i, and S_i at the beginning of cycling were obtained either from open literature or from the technical information provided by the manufacturer (MSA) of the battery and are shown in Table I. As the cell ages, the number of parameter values known a priori is drastically reduced. Such unknown parameter values for a model can be estimated using the model to fit the experimental data using a nonlinear least-squares regression technique such as the Marquardt method.[25,28] We previously illustrated[25] the suitability of nonlinear regression to obtain parameter values from the charge/discharge curves.

Table I. Physical properties of the electrolyte and the electrodes of the lithium-ion cell used in this work.

	Cathode	Anode	Reference
$c_{i,max}$	5.1555×10^{-2} mol/cm^3	3.0555×10^{-2} mol/cm^3	16–18
R_i	11.0×10^{-4} cm	12.5×10^{-4} cm	m[a]
$w_{i,0}$	15.92 g/cell	7.472 g/cell	m[a]
$S_i = 3w_i/(R_i/\rho_i)$	8666.3 cm^2	7934.9 cm^2	Calculated
C_{sp}	274 mAh/g	372 mAh/g	m[a]
c_e	1.0×10^{-3} mol/cm^3	1.0×10^{-3} mol/cm^3	m[a]
T	308.15	308.15	Test condition

[a] Manufacturer's data.

In the present study, only the constant current portions of the discharge profiles were considered for estimation of the parameter values. Consequently, the values for the initial states of charge (i.e., $\theta_{p,0}$ and $\theta_{n,0}$) become very important parameters because the capacity supplied or obtained from the cell during the constant voltage part is not known accurately. Hence, in this work, the initial states of change were treated as fitting parameters. In estimating parameter values from fresh cells[25] that were not subject to cycling (other than the initial formation cycles), the active material loading in each electrode was provided by the manufacturer and was also verified using half-cell studies. However, when using data from cycled electrodes, additional difficulties appear, because the values of the actual weight of usable active material within each electrode are unknown. Hence, these need to be estimated as additional parameters as well. A nonlinear least-squares regression technique called the Levenberg—Marquardt method was used to fit the charge and discharge data and obtain parameter estimates.[25,28,29] This method was previously used by us to fit the experimental cell voltage vs current density (*V-I*) data for a polymer electrolyte membrane fuel cell cathode.[29] In general, the Marquardt method is associated with finding the parameter correction vector $\Delta\boldsymbol{\theta}$ [28]

$$\Delta\boldsymbol{\theta} = (\lambda\mathbf{I} + \mathbf{J}^T\mathbf{J})^{-1}\mathbf{J}^T(\mathbf{Y}^* - \mathbf{Y}) \quad [12]$$

where $\mathbf{J}$ is a matrix of the partial derivatives of the cell voltage (dependent variable) with respect to all the fitting parameters θ_i evaluated at all the experimental data, $\mathbf{Y}$ is a vector of the predicted values of the cell voltage, $\mathbf{Y}^*$ is a vector of the experimental values of the cell voltage, λ is the step-size correction factor which is assigned a large value of 100 initially in the regression and a very small value upon convergence, i.e., 10^{-6},[28] $\mathbf{I}$ is an identity matrix, and the superscripts T and -1 represent the transpose and the inverse of a matrix, respectively. In Eq. 18, the elements of $\mathbf{J}$ can be calculated as follows

$$J_{ij} = [\partial(\Phi_{1,p} - \Phi_{1,n})/\partial\theta_i]_j \quad [13]$$

where i represents the *i*th fitting parameter, j represents the *j*th data point, and J_{ij} is the sensitivity of the cell voltage to a change in the value of parameter θ_i evaluated at the *j*th data point. The values of the entries in the matrix $\mathbf{J}$ are calculated using the sensitivity approach. Further details on this approach were provided in an earlier work.[25] All the sensitivity equations and model equations were solved simultaneously. The total number of sensitivity equations to be solved in least-squares regression is the number of model equations times the number of fitting parameters. The regression converges when either each element in $\Delta\boldsymbol{\theta}$ has a negligible value or the standard deviation of the predicted value of the cell voltage from the experimental value, S_E, does not change appreciably from iteration to iteration.[28] The value of S_E is calculated using

Table II. Experimental capacities measured after every 100 cycles for five different cells cycled at 5, 15, 25, 35, and 45°C.

	Fresh	Cycle 100	Cycle 200	Cycle 300	Cycle 400	Cycle 500
5°C	1.8867	1.7454	1.6723	1.6031	1.5522	1.4705
15°C	1.9870	1.7891	1.6094	1.4227	1.2143	0.9730
25°C	1.9667	1.7367	1.4567	1.1867	0.9467	0.7367
35°C	1.9667	1.3466	0.6667	—	—	—
45°C	1.9667	0.8667	0.2467	—	—	—

$$S_E = \sqrt{\frac{1}{N - n_\theta}\sum_{j=1}^{N}[(V_{Cell})_j - (V_{Cell})_j^*]^2} \qquad [14]$$

where N is the total number of experimental data points, n_θ is the number of fitting parameters, and $(V_{Cell})_j$ and $(V_{Cell})_j^*$ are the predicted and experimental values of the cell voltage, respectively, at the jth data point.

Statistically, the confidence intervals for the fitting parameters are more useful than their point estimates. In this work, the 95% confidence interval for parameter θ_i was constructed as follows[28]

$$\theta_i^* - t_{(1-0.05/2)}S_E\sqrt{a_{ii}} \leq \theta_i < \theta_i^* + t_{(1-0.05/2)}S_E\sqrt{a_{ii}} \qquad [15]$$

where θ_i^* is the point estimate for parameter θ_i, $t_{(1-0.05/2)}$ is the value of Student's t distribution with $(N\text{-}n_\theta)$ degrees of freedom and 95% confidence, and a_{ii} is the ith element of the principal diagonal of $(\mathbf{J}^T\mathbf{J})^{-1}$ using the values of S_E given by Eq. 14.

Results and Discussion

The charge and discharge data of a lithium-ion battery depend strongly on the OCP equations of both the cathode and anode. In general, the OCP data of an intercalation electrode cannot be predicted using a Nernst equation due to the existence of voltage plateaus corresponding to different stages of intercalation. Because of this, the equations used in the literature to fit the OCP data of an intercalation electrode vary widely.[1-18] Among them, functional terms are usually employed to capture a change in the OCP profile with the SOC of the electrode.[1-15] We used cubic splines[30] and piecewise polynomials[31] to fit the OCP data of the lithium cobalt oxide cathode and those of the carbon anode measured via a half-cell setup consisting of an intercalation electrode and a lithium foil. The OCP equations used in this work were based on the cubic spline fitting carried out earlier and are presented in the Appendix of Santhanagopalan et al.[25] Figures 2 and 3 show that the experimentally measured OCP data agree with the spline fit very well. Liaw et al. have proposed a change in the OCV curves with cycling.[20] The diffusion and kinetic constants are also reported to change with time. However, in the present work, it was assumed that the OCVs, as well as the transport and kinetic rate constants, do not change as the cell ages. This assumption aids in reducing the number of parameters to be estimated simultaneously.

Fitting cycling data.— Obtaining the correct set of initial values for all the parameters before the iterations is a tedious task. In order to overcome this difficulty, the data from cycle one at the *C*/33 rate at each temperature was first fit to the particle model described above. These values for the parameters were then used as the initial guess values for the subsequent cycles at the corresponding temperatures. The experimental capacity of each cell after every 100 cycles is shown in Table II. As observed, the remnant capacity in cells cycled at 35 and 45°C was very small. Hence, testing of these cells was stopped after 200 cycles. In obtaining the fits it was assumed that there are no kinetic and transport limitations during this slow rate discharge. Hence, the values for the diffusion and reaction coefficients were held constant as shown in Table III. Estimates for these parameters were obtained previously using charge–discharge curves from fresh cells at various rates.[25] There were four parameters used to fit the discharge curve at each cycle: the SOC of each electrode at the beginning of discharge ($\theta_{p,0}$ and $\theta_{n,0}$) and the weight of the active material accessible during each cycle (w_p and w_n). Table IV shows the values for the parameters estimated at each temperature. Also shown are the confidence intervals for each parameter.

Figure 4 shows the comparison between the experimental data and the model fits at each temperature. The experimental data is represented by continuous lines and the model prediction by the symbols. At 5°C, the total capacity loss after 500 cycles is less than 20%, and the corresponding change in the parameter values is also relatively small. At 15 and 25°C, there is a very good fit for data up to 200 cycles. Beyond that, holding the transport and the kinetic parameters constant does not yield good fits. The capacity of the cell matches that of the model, and the initial states of charge from the model are in good agreement with the data; however, the change in the shape of the discharge curve could not be captured using the above model. This result can be explained as follows: after 200 cycles the cell loses a lot of capacity and the current based on the initial SOC (i.e., 0.05 A) is much larger than the *C*/33 rate. As a result, kinetic and transport limitations set in, similar to a higher rate discharge. This also explains the larger confidence intervals in Table IV for the parameters estimated at 15 and 25°C for cycles 200 or more. At higher temperatures, the capacity loss is predominantly due to the loss of active material (see Table IV). Because the model does capture the change in the weight of the active material, the fits are reasonable at the higher temperatures.

Loss of active material vs loss of cyclable lithium.— The loss of capacity in a cell can originate from the loss of cyclable lithium or the loss of active material in itself.[19] For example, as seen from Table V, the capacity fade during the first 100 cycles at 15°C is dominated by the loss of active lithium at the anode. This is quickly replaced by the loss of lithium at the cathode. At 25°C, the first few cycles experience a loss of lithium at the anode (e.g., due to the formation of a film); at cycles 100–200 the change in the SOC of the cathode is drastic, indicating an increase in the impedance at the positive electrode. Only toward the end of 500 cycles, the loss of active material at the anode plays a significant role in the capacity fade at 25°C. The capacity fade due to loss of active material contributes to less than 1% of the total capacity loss at 5°C. However, at higher temperatures (35 and 45°C), the capacity fade is predominantly controlled by the rapid loss of active material at the anode.

In order to compare the relative contributions of the loss of cyclable lithium and that of accessible active material, we now define a *scaled* initial SOC (x_i) within each electrode as the ratio between

Table III. Values of the parameters estimated[a] from rate capability data on a fresh cell for use in estimation of parameters from the *C*/33 rate data.

Parameter	Value
$D_{1,p}$ (cm^2/s)	0.43334×10^{-10}
$D_{1,n}$ (cm^2/s)	0.13833×10^{-10}
k_p [A/cm^2/(mol/cm^3)$^{1.5}$]	2.3632
k_n [A/cm^2/(mol/cm^3)$^{1.5}$]	0.25195

[a] Reference 25.

Table IV. Estimated values for the parameters as a function of cycle number and the associated 95% confidence intervals.

5°C	Fresh	Cycle 100	Cycle 200	Cycle 300	Cycle 400	Cycle 500
w_p (g)	16.128 ± 0.8421	16.12 ± 1.0137	16.115 ± 1.1019	16.0904 ± 1.5855	16.067 ± 0.0801	16.049 ± 0.1805
w_n (g)	7.472 ± 0.6979	7.4688 ± 0.3122	7.4661 ± 0.5722	7.452 ± 0.2374	7.4487 ± 0.1311	7.4352 ± 0.0643
$\theta_{p,0}$	0.4610 ± 0.0199	0.4659 ± 0.3205	0.4859 ± 0.2369	0.5088 ± 0.3722	0.5224 ± 0.1193	0.5488 ± 0.0596
$\theta_{n,0}$	0.8345 ± 0.0073	0.4880 ± 0.1189	0.2970 ± 0.2381	0.2776 ± 0.2663	0.2681 ± 0.2468	0.2585 ± 0.7147
15°C						
w_p (g)	16.121 ± 0.6100	14.922 ± 0.6194	14.712 ± 0.4203	14.606 ± 0.8867	13.457 ± 0.8525	12.157 ± 0.4343
w_n (g)	7.4473 ± 0.1416	7.1472 ± 3.0551	6.7150 ± 5.0114	6.2790 ± 6.3492	5.6486 ± 3.4200	4.9169 ± 2.4178
$\theta_{p,0}$	0.4711 ± 0.02523	0.5076 ± 0.1328	0.5359 ± 0.3171	0.6114 ± 0.1202	0.6203 ± 0.6127	0.6602 ± 0.5650
$\theta_{n,0}$	0.8243 ± 0.0777	0.3105 ± 0.14519	0.2276 ± 0.5152	0.2170 ± 0.2010	0.2067 ± 0.0807	0.1965 ± 0.0173
25°C						
w_p (g)	16.148 ± 1.5528	16.061 ± 1.1199	15.721 ± 0.7589	14.827 ± 0.8129	14.123 ± 0.9425	13.512 ± 1.7147
w_n (g)	7.4503 ± 0.5114	7.4422 ± 3.6073	7.4316 ± 5.1515	6.6762 ± 7.3187	5.9740 ± 3.1874	5.3382 ± 1.4252
$\theta_{p,0}$	0.4831 ± 0.0627	0.5149 ± 0.5082	0.5928 ± 0.7096	0.6338 ± 0.0275	0.6885 ± 0.0526	0.7154 ± 0.2171
$\theta_{n,0}$	0.8273 ± 0.07603	0.2360 ± 0.1894	0.1737 ± 0.2702	0.1684 ± 0.2144	0.1574 ± 0.2019	0.1527 ± 0.2420
35°C						
w_p (g)	16.117 ± 0.5627	14.131 ± 3.3625	10.782 ± 2.3469	—	—	—
w_n (g)	7.4715 ± 1.5957	5.6482 ± 2.3289	3.6723 ± 1.2960	—	—	—
$\theta_{p,0}$	0.4811 ± 0.1046	0.5029 ± 0.3097	0.5555 ± 0.3027	—	—	—
$\theta_{n,0}$	0.8243 ± 0.1097	0.1655 ± 0.2914	0.1557 ± 0.1391	—	—	—
45°C						
w_p (g)	16.122 ± 1.3836	12.729 ± 1.6479	9.732 ± 1.4289	—	—	—
w_n (g)	7.4382 ± 0.8537	4.2576 ± 2.7315	2.2632 ± 1.9971	—	—	—
$\theta_{p,0}$	0.4861 ± 0.2905	0.5255 ± 0.4643	0.5851 ± 0.3496	—	—	—
$\theta_{n,0}$	0.8257 ± 0.0804	0.1393 ± 0.1987	0.1243 ± 0.0834	—	—	—

the dimensionless concentration of lithium inside the electrode i to the dimensionless weight of the active material

$$x_i = \frac{c_i/c_{i,\max}}{w_i/w_{i,0}} \quad [16]$$

The parameter $w_{i,0}$ denotes the weight of active material at the beginning of cycle 1 in electrode I, and the values for $w_{p,0}$ and $w_{n,0}$ are shown in Table I. The variable x_i gives the ratio between the capacity from cyclable lithium and that from the active material. For cycle 1, $w_i = w_{i,0}$ and hence, x_i holds the same significance as θ_i (the dimensionless concentration of lithium inside electrode i). Figure 5 shows the value of x_i at the beginning of every hundred cycles within each electrode. For the cathode, a shift in the value of x_i between two cycles to the left indicates that the change value of θ_i is less than the corresponding change in the value of w_i between those two cycles, i.e., the loss of active material supersedes the loss of cyclable lithium. A shift of x_i to the right inside the cathode indicates that the loss of cyclable lithium overcomes the loss of active material. At the anode, the reverse is true: a shift in the value of x_i to the left indicates that changes in the value of θ_i are less than the corresponding changes in the value of w_i between those two cycles. In these cases, the available active material is not utilized to its maximum capacity. However, a shift in the value of x_i to the right indicates that the loss of active material overcomes the capacity fade

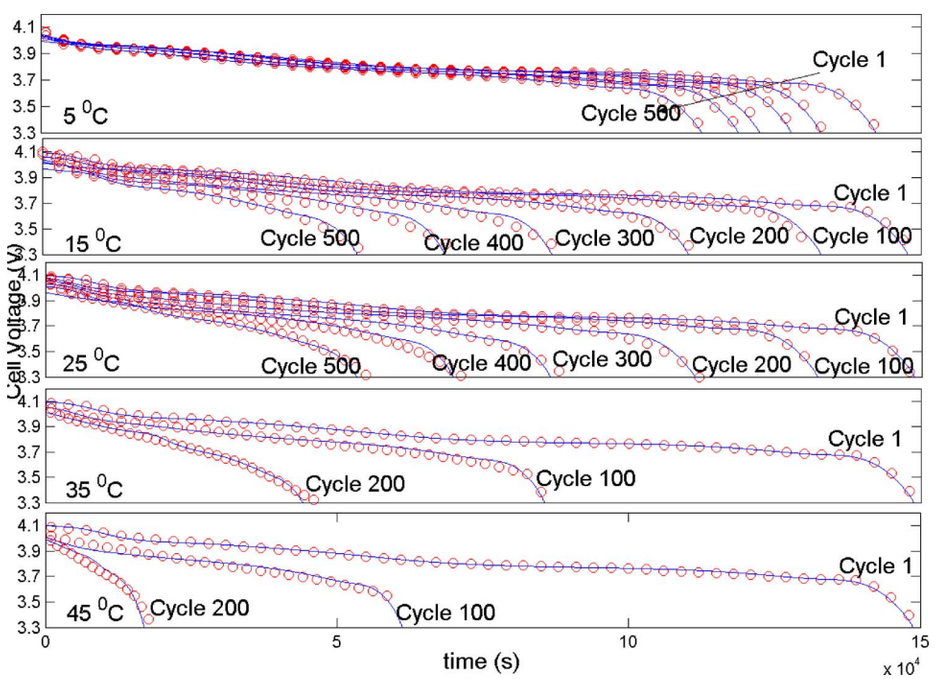

Figure 4. (Color online) Comparison of the predictions from the single particle model to the experimental data at the *C*/33 rate. Solid lines indicate experimental data and the symbols indicate the model predictions. At 35 and 45°C, the cycling was stopped after 200 cycles since the remaining capacity was very low.

Table V. Capacity lost due to the loss of cyclable lithium and that due to the loss of active material after every 100 cycles at various temperatures.

Total capacity loss	Cycle 100	Cycle 200	Cycle 300	Cycle 400	Cycle 500
5°C	0.1400	0.0700	0.0700	0.0500	0.0800
15°C	0.1981	0.1795	0.1867	0.2084	0.2413
25°C	0.2300	0.2800	0.2700	0.2400	0.2100
35°C	0.6201	0.6799			
45°C	1.1000	0.6200			
w_p losses	Cycle 100	Cycle 200	Cycle 300	Cycle 400	Cycle 500
5°C	0.0012	0.0007	0.0036	0.0035	0.0027
15°C	0.1017	0.0311	0.0157	0.1701	0.1924
25°C	0.0129	0.0502	0.1323	0.1042	0.0904
35°C	0.2941	0.4955			
45°C	0.5022	0.4436			
w_n losses	Cycle 100	Cycle 200	Cycle 300	Cycle 400	Cycle 500
5°C	0.0011	0.0009	0.0048	0.0011	0.0046
15°C	0.1017	0.1465	0.1478	0.2137	0.2480
25°C	0.0027	0.0036	0.2561	0.2380	0.2155
35°C	0.6182	0.6699			
45°C	1.0782	0.6761			
$\theta_{p,0}$ losses	Cycle 100	Cycle 200	Cycle 300	Cycle 400	Cycle 500
5°C	0.0171	0.0653	0.0749	0.0444	0.0859
15°C	0.1388	0.1824	0.1886	0.0276	0.1192
25°C	0.1212	0.2787	0.1466	0.1775	0.0817
35°C	0.0828	0.1213			
45°C	0.1511	0.1089			
$\theta_{n,0}$ losses	Cycle 100	Cycle 200	Cycle 300	Cycle 400	Cycle 500
5°C	0.1175	0.0647	0.0066	0.0032	0.0033
15°C	0.1742	0.0281	0.0036	0.0035	0.0034
25°C	0.2005	0.0211	0.0018	0.0037	0.0016
35°C	0.2233	0.0033			
45°C	0.2327	0.0051			

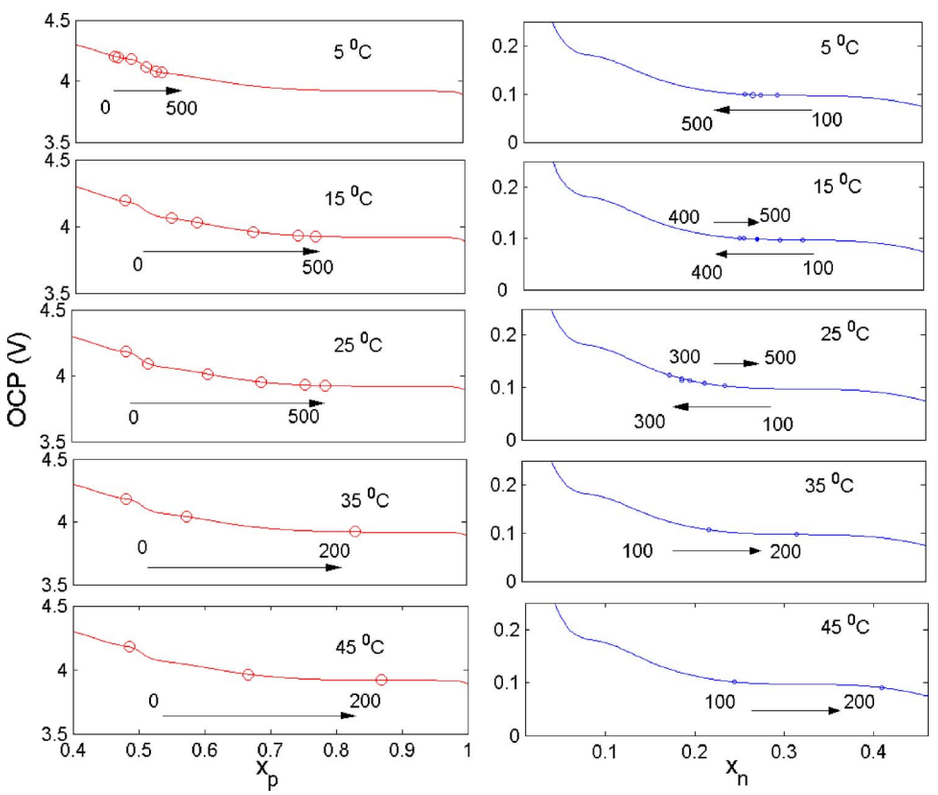

Figure 5. (Color online) Weighted SOC within each electrode as a function of cycle number at various temperatures. A shift toward the left for the cathode indicates that the loss of active material supersedes the loss of cyclable lithium. For the anode, a shift toward the right indicates that the loss of active material is greater than the loss of available lithium. The OCP values are plotted vs x_i for the first cycle [which is the same as $(\theta_i|_{\bar{r}_p=1})$ for cycle 1].

due to the loss of cyclable lithium; hence, the decrease in the amount of accessible active material leads to a better utilization of the active material available at that cycle.

As observed in Fig. 5, the values of x_p do not shift to the left, which indicates that the loss of active material at the cathode is small and does not influence the performance of the cells of this specific design. The extent of shift in the values of x_p between any two cycles is a direct measure of the performance of the cathode and can be used to compare the extent of aging between any two cycles shown. For example, the shift in x_p (Δx_p) between cycles 1 and 500 at 5°C is between 0.4 and 0.6, whereas Δx_p between cycles 1 and 500 at 15°C varies from 0.4 to 0.8, indicating a degradation about twice as fast as that at 5°C. Based on similar arguments, the shift in Δx_i between 15 and 25°C indicates that the degradation at 25°C is similar to the one at 15°C. At higher temperatures, the losses are even higher. However, at all temperatures, the values of x_p shift toward the right, indicating that the loss of active material does not exceed the loss of cyclable lithium. At the anode, the initial values of x_n at cycle 1 for all temperatures is about 0.83 (as seen from Table IV). The first few cycles show a significant loss of cyclable lithium at the anode. As a result, at cycle 100, the values of x_n all shift to 0.3–0.4. For clarity, the open-circuit potential values for x_n values between 0.1 and 0.5 are shown in Fig. 5. At 5°C, the loss of cyclable lithium at the anode supersedes the loss of active material. Hence, the value of x_n shifts toward the left for all cycles. At 15 and 25°C, the values of x_n shift toward the left for the first few hundred cycles; however, the trend is reversed at higher cycle numbers, indicating a critical loss of active material at the anode as the limiting factor. The loss of active material is further aggravated at higher temperatures (35 and 45°C), where degradation due to cyclable lithium loss is restricted to approximately the first 100 cycles. Beyond that, even if excess lithium were to be available, the loss of active material prevents any contribution to the cell capacity and may even lead to the plating of lithium as the potential shifts to lower values.

Quantifying capacity fade.— The total loss of cell capacity after every 100 cycles is shown in Table II. From the discussion in the previous section, it is evident that capacity fade is a combination of several factors that influence the performance of a cell to varying extents, depending on the operating temperature and the age of the cell. In this section, we attempt to quantify the loss of capacity within the cell at each temperature from four different factors: the loss of active material (i.e., change in w_p or w_n) and the loss of cyclable lithium within each electrode (i.e., change in θ_p or θ_n). The decrease in capacity from the loss of active material is calculated using theoretical values for the capacity of the active material (239 mAh/g for the anode and 148 mAh/g for the cathode). Thus, a loss of 1 g of active material at the anode was accounted as a 239 mAh fade in the capacity of the cell. The loss of cyclable lithium was based on the parameters from cycle 1. In other words, a well-balanced cell was assumed to exist at cycle 1 and the initial capacity of the cell was scaled by the change in θ_i after every 100 cycles to calculate the capacity at that cycle. The total capacity loss at each temperature is shown in Table V. Also shown are the capacity losses from the individual factors (i.e., w_p, w_n, θ_p, and θ_n losses).

As seen from Fig. 6-9, these results reinstate the previous arguments shown in Fig. 5 and Table IV. The capacity of the cell is limited for the first few cycles by θ_n losses at all temperatures. The active material loss at the anode (w_n) determines the available capacity at all temperatures toward the end of life. At 15 and 25°C, the effect of changes in θ_p can be seen. Note that for each case, the available cell capacity is limited by the maximum of the capacity losses from the four factors described above. This idea is illustrated in Fig. 6-10 by superimposing the total capacity fade of the cell over the loss due to the individual factors, and at each point, the total capacity loss matches the maximum capacity loss from the individual factors. Any difference between the two arises from the lack of confidence in the parameter values estimated for that case.

Finally, there are some limitations in the results shown above.

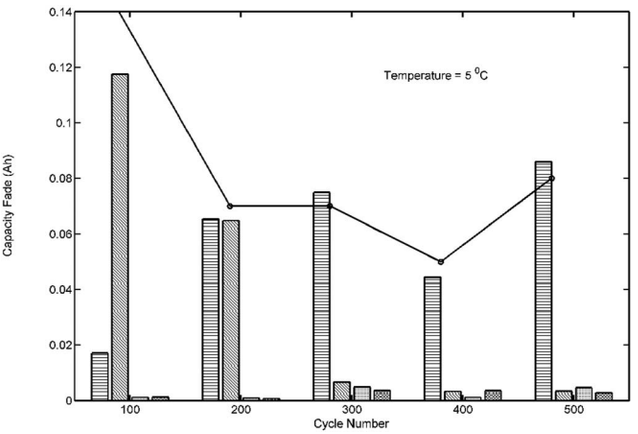

Figure 6. Comparison of capacity fade from various factors after every 100 cycles: ▤ indicates capacity fade due to loss of cyclable lithium at the anode, ▨ indicates capacity fade due to loss of cyclable lithium at the cathode, ▥ indicates capacity fade due to loss of active material at the anode, and ▩ indicates capacity fade due to loss of active material at the cathode. The line indicates the total capacity fade as a function of cycle number at 5°C.

These simulations overestimate the change in the parameters for two reasons: the loss of active material leads to the current (0.828 A) being much higher than the *C*/2 rate. Hence, it is more appropriate to use models including gradients in the solution phase. Also, these simulation results rely heavily on the *C*/33 rate estimates of the amount of active material and the initial states of charge. Hence, limitations from the *C*/33 rate simulations apply. Also, the question of uniqueness of the set of parameter values obtained remains open. Nevertheless, the good confidence intervals for the parameter values are indicative of the fact that the estimation does yield one set of parameters that are significant. The estimates of the initial SOCs and the active material loss must be validated against half-cell data from cycled cells. No attempt has been made to propose a mechanism for any loss in capacity. While there exist several capacity fade mechanisms in the literature, no attempt was made to validate one mechanism against any other.

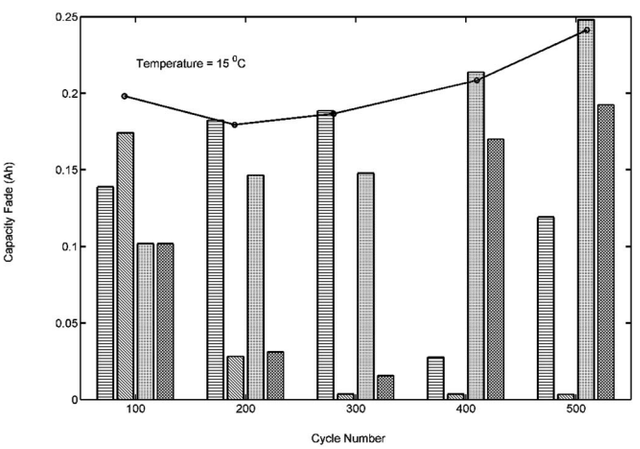

Figure 7. Comparison of capacity fade from various factors after every 100 cycles: ▤ indicates capacity fade due to loss of cyclable lithium at the anode, ▨ indicates capacity fade due to loss of cyclable lithium at the cathode, ▥ indicates capacity fade due to loss of active material at the anode, and ▩ indicates capacity fade due to loss of active material at the cathode. The line indicates the total capacity fade as a function of cycle number at 15°C.

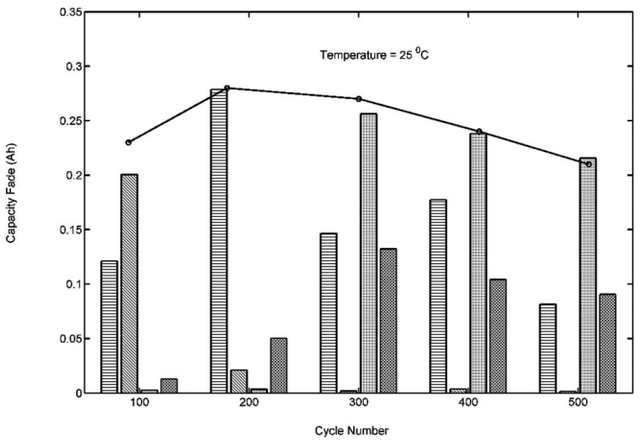

Figure 8. Comparison of capacity fade from various factors after every 100 cycles: ▤ indicates capacity fade due to loss of cyclable lithium at the anode, ▨ indicates capacity fade due to loss of cyclable lithium at the cathode, ⬚ indicates capacity fade due to loss of active material at the anode, and ▩ indicates capacity fade due to loss of active material at the cathode. The line indicates the total capacity fade as a function of cycle number at 25°C.

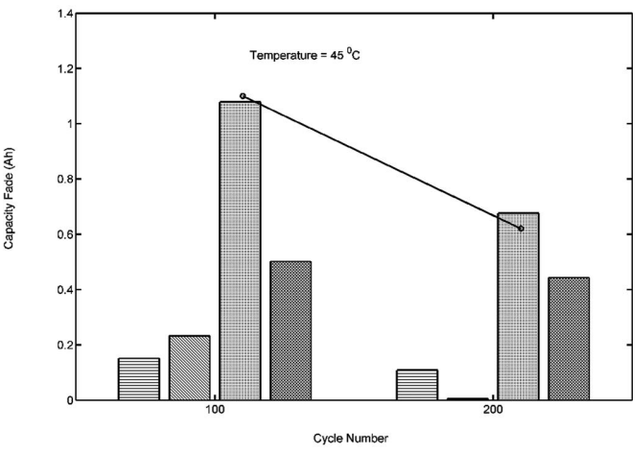

Figure 10. Comparison of capacity fade from various factors after every 100 cycles: ▤ indicates capacity fade due to loss of cyclable lithium at the anode, ▨ indicates capacity fade due to loss of cyclable lithium at the cathode, ⬚ indicates capacity fade due to loss of active material at the anode, and ▩ indicates capacity fade due to loss of active material at the cathode. The line indicates the total capacity fade as a function of cycle number at 45°C.

Conclusions

A simple physics-based model was used to obtain the change in the amount of cyclable lithium and the amount of active material loss in each electrode of a lithium-ion cell. The results indicate that the capacity fade is influenced by a combination of these factors. For the cells studied here, the contribution to capacity fade from the cathode is not significant. The loss of cyclable lithium influences the first few cycles and then the loss of active material at the anode takes over as the limiting factor that determines the performance of the cell. The changes in the shape of the discharge curve are not captured by the model presented here. A more sophisticated model including either solution phase resistance or other mechanisms might be used to predict these changes. Also, the present work here does not provide a specific mechanism for the loss of either cyclable lithium or that of the accessible active material. However, the work presented here does illustrate that the change in the accessible amount of active material is significant with cycling and hence should be included in a mechanistic model that explains capacity fade.

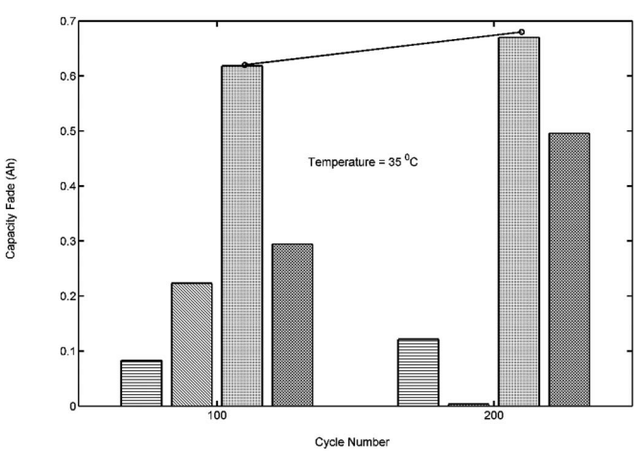

Figure 9. Comparison of capacity fade from various factors after every 100 cycles: ▤ indicates capacity fade due to loss of cyclable lithium at the anode, ▨ indicates capacity fade due to loss of cyclable lithium at the cathode, ⬚ indicates capacity fade due to loss of active material at the anode, and ▩ indicates capacity fade due to loss of active material at the cathode. The line indicates the total capacity fade as a function of cycle number at 35°C.

Acknowledgment

The authors are grateful for the financial support of the project from the National Reconnaissance Office (NRO) under contract no. NRO-000-03-C-0122.

The University of South Carolina assisted in meeting the publication costs of this article.

List of Symbols

a_{ii}	ith element of the principal diagonal of $(\boldsymbol{J}^T\boldsymbol{J})^{-1}$
c_i	concentration of lithium ions in the intercalation particle of electrode i, mol/cm^3
$c_{i,max}$	maximum concentration of lithium ions in the intercalation particle of electrode i, mol/cm^3
c_e	concentration of the electrolyte, mol/cm^3
C	capacity of the cell, Ah
D_i	solid phase diffusion coefficient of lithium ions in the intercalation particle of electrode i, cm^2/s
F	Faraday's constant, 96,487 C/equiv
I	charge or discharge current, A
I_{app}	applied current, A
$i_{0,p}$	exchange current density for the cathode, A/cm^2
$\boldsymbol{J}$	Jacobian matrix for parameter estimation
J_i	flux of lithium ions for the electrochemical reaction on the surface of the intercalation particle of electrode i, mol/cm^2/s
k_i	rate constant for the electrochemical reaction of electrode i, (mol/cm^2/s)/(mol$^{1.5}$/cm$^{4.5}$)
N	total number of data points
n	negative electrode
n_θ	number of parameters estimated
p	positive electrode
$\bar{r}_i$	coordinate in the spherical intercalation particle of electrode i normalized by the radius of that particle, $0 \le \bar{r}_i \le 1$
R	gas constant, 8.3143 J/(mol·K)
R_i	radius of the spherical intercalation particle of electrode i, cm
S_i	total electroactive surface area of electrode i, cm^2
S_E	standard deviation, V
t	time, s
$t_{(1-0.05/2)}$	value of the student's t distribution with (N-m) degrees of freedom
U_i	open-circuit potential of electrode i, V
w_i	weight of the active material of electrode i, g
x_i	weighted initial SOC of the electrode i

$\mathbf{Y}$ vector of the predicted values of the dependent variable evaluated at all the experimental data points of all the discharge curves, V
$\mathbf{Y}^*$ vector of all the experimental values of the dependent variable of all the discharge curves, V

Greek

η_i overpotential of the desired electrochemical reaction of electrode i, V
$\boldsymbol{\theta}$ vector of fitting parameters
θ_i dimensionless concentration of lithium inside electrode i
$\theta_{i,0}$ dimensionless concentration of lithium inside electrode i at the beginning of discharge
θ_i *i*th fitting parameter
θ_i^* point estimate of parameter θ_i
λ step-size correction factor in the regression, which is assigned a value of 100 as the beginning of the regression
$\Phi_{1,i}$ solid phase potential of electrode i, V

References

1. W. A. van Schalkwijk and B. Scrosati, *Advances in Lithium-Ion Batteries*, Kluwer Academic/Plenum Publishers, New York (2002).
2. T. F. Fuller, M. Doyle, and J. Newman, *J. Electrochem. Soc.*, **141**, 1 (1994).
3. M. Doyle and J. Newman, *Electrochim. Acta*, **40**, 2191 (1995).
4. G. Sikha, P. Ramadass, B. S. Haran, R. E. White, and B. N. Popov, *J. Power Sources*, **122**, 67 (2003).
5. K. Kumaresan, Q. Guo, P. Ramadass, and R. E. White, *J. Power Sources*, **158**, 679 (2006).
6. M. C. Smart, J. F. Whitacre, B. V. Ratnakumar, and K. Amine, *J. Power Sources*, **168**, 501 (2007).
7. D. H. Doughty, P. C. Butler, R. G. Jungst, and P. E. Roth, *J. Power Sources*, **110**, 357 (2002).
8. P. Arora, M. Doyle, A. S. Gozdz, R. E. White, and J. Newman, *J. Power Sources*, **88**, 219 (2000).
9. V. Srinivasan and C. Y. Wang, *J. Electrochem. Soc.*, **150**, A98 (2003).
10. C. Y. Wang, W. B. Gu, and B. Y. Liaw, *J. Electrochem. Soc.*, **145**, 3407 (1998).
11. V. R. Subramanian, V. Diwakar, and D. Tapriyal, *J. Electrochem. Soc.*, **152**, A2002 (2005).
12. P. Arora, M. Doyle, and R. E. White, *J. Electrochem. Soc.*, **146**, 3543 (1999).
13. P. Arora, R. E. White, and M. Doyle, *J. Electrochem. Soc.*, **145**, 3647 (1998).
14. M. Verbrugge and B. J. Koch, *J. Power Sources*, **110**, 295 (2002).
15. B. Y. Liaw, R. G. Jungst, G. Nagasubramanian, H. L. Case, and D. H. Doughty, *J. Power Sources*, **119–121**, 874 (2003).
16. M. Verbrugge and B. Koch, *J. Electrochem. Soc.*, **153**, A187 (2006).
17. P. Ramadass, B. Haran, P. M. Gomadam, R. E. White, and B. N. Popov, *J. Electrochem. Soc.*, **151**, A196 (2004).
18. H. J. Ploehn, P. Ramadass, and R. E. White, *J. Electrochem. Soc.*, **151**, A456 (2004).
19. P. Ramadass, B. Haran, R. E. White, and B. N. Popov, *J. Power Sources*, **123**, 230 (2003).
20. B. Y. Liaw, R. G. Jungst, G. Nagasubramanian, H. L. Case, and D. H. Doughty, *J. Power Sources*, **140**, 157 (2005).
21. J. Ihonen, F. Jaouen, G. Lindbergh, A. Lundblad, and G. Sundholm, *J. Electrochem. Soc.*, **149**, A448 (2002).
22. J. N. Reimers and J. R. Dahn, *J. Electrochem. Soc.*, **139**, 2091 (1992).
23. R. Barnard, C. F. Randell, and F. L. Tye, *J. Appl. Electrochem.*, **10**, 109 (1980).
24. K. Dokko, M. Mohamedi, Y. Fujita, T. Itoh, M. Nishizawa, M. Umeda, and I. Uchida, *J. Electrochem. Soc.*, **148**, A422 (2001).
25. S. Santhanagopalan, Q. Guo, and R. E. White, *J. Electrochem. Soc.*, **154**, A198 (2007).
26. S. Santhanagopalan, Q. Guo, P. Ramadass, and R. E. White, *J. Power Sources*, **156**, 620 (2006).
27. B. Wu and R. E. White, *Comput. Chem. Eng.*, **25**, 301 (2001).
28. A. Constantinides and N. Mostoufi, *Numerical Methods for Chemical Engineers with MATLAB Applications*, Prentice Hall, Upper Saddle River, NJ (1999).
29. Q. Guo, V. A. Sethuraman, and R. E. White, *J. Electrochem. Soc.*, **151**, A983 (2004).
30. Q. Guo and R. E. White, *J. Electrochem. Soc.*, **152**, A343 (2005).
31. A. T. Stamps, S. Santhanagopalan, and E. P. Gatzke, *J. Electrochem. Soc.*, **154**, P20 (2007).